OPEN ACCESS



Stream-aligned Magnetohydrodynamics for Solar Wind Simulations

Igor V. Sokolov[®], Lulu Zhao[®], and Tamas I. Gombosi[®]

Department of Climate and Space Sciences and Engineering, University of Michigan, 2455 Hayward St., Ann Arbor, MI 48109, USA; igorsok@umich.edu Received 2021 October 18; revised 2021 November 27; accepted 2021 December 2; published 2022 February 16

Abstract

We present a reduced magnetohydrodynamic (MHD) mathematical model describing the dynamical behavior of highly conducting plasmas with frozen-in magnetic fields, constrained by the assumption that there exists a frame of reference, where the magnetic field vector, \mathbf{B} , is aligned with the plasma velocity vector, \mathbf{u} , at each point. We call this solution "stream-aligned MHD" (SA-MHD). Within the framework of this model, the electric field, $\mathbf{E} = -\mathbf{u} \times \mathbf{B} \equiv 0$, in the induction equation vanishes identically and so does the electromagnetic energy flux (Poynting flux), $\mathbf{E} \times \mathbf{B} \equiv 0$, in the energy equation. At the same time, the force effect from the magnetic field on the plasma motion (the Ampère force) is fully taken into account in the momentum equation. Any steady-state solution of the proposed model is a legitimate solution of the full MHD system of equations. However, the converse statement is not true: in an arbitrary steady-state magnetic field, the electric field does not have to vanish identically (its curl has to, though). Specifically, realistic three-dimensional solutions for the steady-state ("ambient") solar atmosphere in the form of so-called Parker spirals can be efficiently generated within the stream-aligned MHD (SA-MHD) with no loss in generality.

Unified Astronomy Thesaurus concepts: Solar wind (1534); Corotating streams (314); Solar corona (1483)

1. Introduction

Space weather describes the dynamic state of the Earth's magnetosphere-ionosphere system, which is driven by solar wind and solar ionizing radiation. The greatest disturbances in space weather are geomagnetic storms, the most severe of which are caused by coronal mass ejections (CMEs) (see Gosling 1993). To simulate, forecast, or just nowcast space weather events, which from a mathematical standpoint are essentially time-dependent processes, global models are needed to simulate, as the initial stage, the steady state of the solarterrestrial environments. The resulting solution for the "preevent" solar wind and terrestrial magnetosphere serves as the background through which the space weather disturbance propagates and shocks and discontinuities are generated. The solar energetic particle (SEP) transport, as well as the formation of their seed population, is mostly controlled by this background solution as well.

In realistic solar atmosphere simulations, the essentially three-dimensional (3D) interplanetary magnetic field can be steady state only in coordinate systems corotating with the Sun (such as HGR). In corotating frames, solar active regions and coronal holes, which are mostly responsible for shaping the structure of the solar atmosphere, can be treated as steady-state sources. Despite being steady-state globally, the solution for the solar wind is highly variable at Earth's location, since in any corotating system the Earth orbits the Sun with the Carrington rotation period. This relative motion allows us to compare time series of solar wind parameters observed by Earth or L1 orbiting spacecraft, $SW_{observed}(t)$, with the simulated steady-state parameters for the 3D background solar wind, $SW_{background}(\mathbf{R})$, by extracting the time series of simulated values, $SW_{background}(\mathbf{R}_{Earth_HGR}(t))$, at the timedependent Earth location in the HGR system, $R_{\text{Earth HGR}}(t)$.

Original content from this work may be used under the terms of the Creative Commons Attribution 4.0 licence. Any further distribution of this work must maintain attribution to the author(s) and the title of the work, journal citation and DOI.

The time series of observations by the two STEREO spacecraft provide additional validation possibilities.

In the last two decades, several 3D solar wind (Usmanov et al. 2000; Suzuki & Inutsuka 2005; Verdini et al. 2009; Osman et al. 2011; Lionello et al. 2014a, 2014b; Usmanov et al. 2018) and coronal heating models (Tu & Marsch 1997; Hu et al. 2000; Dmitruk et al. 2002; Li & Habbal 2003; Cranmer 2010) that included, or were exclusively driven by, Alfvén wave turbulence became increasingly popular. Our group also includes Alfvén wave turbulence in our corona and inner heliosphere model (see, e.g., Sokolov et al. 2013, 2021a; Oran et al. 2013; van der Holst et al. 2014; Gombosi et al. 2018, 2021). Although popular, this physics-based approach to modeling the background solar wind is not the only way to model the solar corona and the solar wind. Empirical descriptions of the solar wind, like the widely used Wang-Sheeley-Arge (WSA) model (Arge & Pizzo 2000), are also attractive because of their simplicity and ability to predict the solar wind speed in the inner heliosphere. In addition, the WSA formalism can be readily incorporated into global 3D models for the solar corona and inner heliosphere, e.g., via a varying polytropic index distribution (see Cohen et al. 2006), as proposed by Roussev et al. (2003), or via the boundary condition set at the solar surface (Shen et al. 2018) or at 0.1 au (see, e.g., Pomoell & Poedts 2018).

There is, however, a conceptual difference between global solar atmosphere models that are based on numerical solutions of the ideal (or resistive) MHD equations and simple (but efficient) semianalytic solar wind models that imply a classical Parker-spiral structure for the interplanetary magnetic field lines. Specifically, in semianalytic models, it is assumed that in the corotating frame of reference under steady-state conditions the solar wind velocity vector u(R) is always aligned (parallel or antiparallel) with the interplanetary magnetic field vector, B(R). This means that streamlines and magnetic field lines are always identical and they form Archimedean or Parker (1958) spirals. The assumed coincidence of solar wind streamlines and interplanetary magnetic field lines (in corotating frames) is at

the heart of almost all analytic, semianalytic, semiempirical, and empirical models of interplanetary space. This assumption results in simple methods for tracing interplanetary magnetic field lines from any point of interest in the solar system back to the Sun. One can just trace back a Parker spiral to find out where the local solar wind and magnetic field line originates from on the Sun. For instance, in the WSA semiempirical model (Arge & Pizzo 2000), this assumption is used to relate the Earth's location to the point on the source surface at which to extract the parameters, predicted by the model.

The problem with the concept of aligned interplanetary streamlines and magnetic field lines is that numerical solutions of the full set of MHD equations have not been able to reproduce this feature so far. Full MHD numerical solutions of the solar atmosphere obtained within the framework of regular MHD are not stream aligned. Even if the initial conditions describe parallel **B** and **u** vectors, the smallest numerical error (such as truncation, finite representation, etc.) will result in uncontrollable growth of misalignment. One of the reasons for this discrepancy is the numerical reconnection across the heliospheric current sheet near the top of helmet streamers: the reconnected field is directed across the current sheet, while the global solar wind streams along with the current sheet, thus resulting in significant misalignment. Within regular MHD there is no mechanism to reestablish the streamline field line alignment.

Tracing magnetic field lines from a point of interest in the heliosphere to the solar surface (*magnetic connectivity*) is needed to identify the point of origin of the magnetic field line. This same magnetic connectivity is also necessary to solve the field-aligned transport of energetic particles that create space radiation hazards. With standard computational MHD calculating the magnetic connectivity can become so challenging that sometimes it is preferable to trace streamlines instead, or even Lagrangian trajectories of fluid elements.

In this paper we present a new global model of the solar atmosphere/solar wind system using a reduced MHD model which ensures stream-aligned magnetic field under steady-state conditions. We call this solution "stream-aligned MHD" (SA-MHD). In this reduced set of MHD equations the electric field, $E = -u \times B \equiv 0$, identically vanishes in the induction equation and so does the electromagnetic energy flux (Poynting flux) in the energy equation, $E \times B \equiv 0$. At the same time, the impact of the magnetic force on the plasma motion (the Ampère force) is explicitly enforced in the momentum equation. It must be emphasized that any steady-state solution of the reduced equation set is a solution of the full MHD system of equations. However, the converse statement is not true, since in an arbitrary steady-state magnetic field the electric field does not have to vanish identically (though its curl must). The main point is that the practically interesting Parker (1958) spiral solutions for the steady-state background solar atmosphere and solar wind can be efficiently generated within the SA-MHD with no loss of generality, in 3D geometry with a realistic solar magnetic field.

2. Full 3D MHD Equations of the Global Model

2.1. Standard MHD Equations with Nonzero Magnetic Field Divergence

Global models of the solar atmosphere are usually based on the standard MHD equations (nonspecified notations are as usual):

$$\partial_t \rho + \overline{\nabla} \cdot (\rho \mathbf{u}) = 0, \tag{1a}$$

$$\partial_t \mathbf{B} + \overline{\nabla} \cdot (\mathbf{u}\mathbf{B} - \mathbf{B}\mathbf{u}) = -\mathbf{u}(\overline{\nabla} \cdot \mathbf{B}), \tag{1b}$$

$$\partial_{t}(\rho \boldsymbol{u}) + \overline{\nabla} \cdot \left[\rho \boldsymbol{u} \boldsymbol{u} - \frac{\boldsymbol{B} \boldsymbol{B}}{\mu_{0}} + \left(P + \frac{B^{2}}{2\mu_{0}} \right) \hat{\boldsymbol{I}} \right] = -\frac{1}{\mu_{0}} \boldsymbol{B}(\overline{\nabla} \cdot \boldsymbol{B}), \tag{1c}$$

$$\partial_{t} \left(\frac{\rho u^{2}}{2} + \frac{P}{\gamma - 1} + \frac{B^{2}}{2\mu_{0}} \right) + \overline{\nabla} \cdot \left[\left(\frac{\rho u^{2}}{2} + \frac{\gamma P}{\gamma - 1} \right) \boldsymbol{u} \right] + \overline{\nabla} \cdot \left[\frac{(\boldsymbol{u}\boldsymbol{B} - \boldsymbol{B}\boldsymbol{u}) \cdot \boldsymbol{B}}{\mu_{0}} \right] = -\frac{(\boldsymbol{u} \cdot \boldsymbol{B})}{\mu_{0}} (\overline{\nabla} \cdot \boldsymbol{B}), \quad (1d)$$

where $B = |\mathbf{B}|$, $u = |\mathbf{u}|$, and $\hat{\mathbf{I}}$ is the unit tensor. We use the equation of state, $P = 2n_i k_B T$, $\rho = m_p n_i$ for the coronal plasma with the polytropic index, $\gamma = 5/3$. We omitted many important effects (effects of gravity and inertial forces are discussed in Section 3.3 (see Sokolov et al. 2021a for a detailed description of a model used in simulations here) in the governing equations, while we explicitly included terms proportional to the divergence of the magnetic field. If the numerical solution for the magnetic field is not divergence-free (see Godunov 1972; Powell et al. 1999), this approach allows us to handle maintain basic physical properties, such as pressure positivity. Indeed, if one takes Equation 1(d) divided by temperature, T, subtracts the dot product of u/T with Equation 1(c) and the dot product of $B/(\mu_0 T)$ and Equation 1(b) and finally adds Equation 1(a) times $s + \frac{1}{T} \left(\frac{u^2}{2} - h \right)$, an extra conservation law is obtained:

$$\partial_t(\rho s) + \overline{\nabla} \cdot (\rho u s) = 0 \tag{2}$$

(see also Godunov 1961, 1972; Harten et al. 1983; Powell et al. 1999), where s and h are the entropy and enthalpy per unit mass and the thermodynamic equations

$$dh = Tds + \frac{1}{\rho}dP, \qquad h = \frac{\gamma P}{\rho(\gamma - 1)},$$
 (3)

were used. Equation (2) is only valid for smooth solutions and it states that the entropy satisfies the conservation law for a passively advected scalar. At shocks and discontinuities the entropy conservation breaks down, but, entropy can only increase, not decrease. Therefore, the total entropy (its volume integral) does not decrease: $\partial_t \int \rho s dV \geqslant 0$, since the integral of $\partial_t(\rho s)$ over the smooth solution region vanishes due to Gauss' theorem applied to Equation (2), while the discontinuities result in entropy production. A consequence of this entropy property is that for such systems, finite-volume numerical schemes ensure that in the numerical solution the physical entropy does not decrease, and consequently, the pressure can never become negative (should the pressure go to zero, the entropy, $s \propto \log(P)$, would drop to minus infinity).

2.2. Separating the Potential Magnetic Field in the Solar Corona

Realistic models of the 3D coronal magnetic field use boundary conditions taken from full disk photospheric magnetograms incorporating current and past observation results. The potential magnetic field solution provides the minimum free magnetic energy for a given boundary condition, therefore, in the "ambient" (background) solution for the solar wind, the magnetic field is approximately equal to the potential configuration in the proximity of the Sun. Following Ogino & Walker (1984) and Tanaka (1994) (see also Powell et al. 1999; Gombosi et al. 2002), we split the total magnetic field to a potential (\mathbf{B}_0) and nonpotential (\mathbf{B}_1) component $\mathbf{B} = \mathbf{B}_0 + \mathbf{B}_1$. We note that at $R = R_{\odot}$ the *potential* \mathbf{B}_0 field dominates. If we use photospheric maps of the radial magnetic field (B_r) , then the potential B_0 field can be recovered from the observed magnetogram using the Potential Field Source Surface Method (PFSSM) that has been originally described by Altschuler et al. (1977). The Laplace Equation for scalar magnetic potential is solved in terms of spherical harmonics between $R_{\odot} \leqslant R$ and $R \leqslant R_{\rm SS} = 2.5 \, R_{\odot}$ with the given radial gradient of the potential (the observed radial field) at $R = R_{\odot}$ and with vanishing magnetic potential (i.e., purely radial magnetic field) at $R = R_{SS}$. Accordingly, the nonpotential (\mathbf{B}_1) field (used by Sokolov et al. 2013; Oran et al. 2013; van der Holst et al. 2014) satisfies zero boundary conditions for the radial field component, $\mathbf{B}_{1_R} = 0$ at $R = R_{\odot}$.

Using the split magnetic field approach the governing equations become the following (the continuity equation does not change, therefore we do not repeat it here):

$$\partial_{t}\boldsymbol{B}_{1} + \overline{\nabla} \cdot [\boldsymbol{u}(\boldsymbol{B}_{1} + \boldsymbol{B}_{0}) - (\boldsymbol{B}_{1} + \boldsymbol{B}_{0})\boldsymbol{u}] \\
= -\boldsymbol{u}[\overline{\nabla} \cdot (\boldsymbol{B}_{1} + \boldsymbol{B}_{0})], \tag{4a}$$

$$\partial_{t}(\rho\boldsymbol{u}) + \overline{\nabla} \cdot \left[\rho\boldsymbol{u}\boldsymbol{u} - \frac{\boldsymbol{B}_{1}\boldsymbol{B}_{1} + \boldsymbol{B}_{0}\boldsymbol{B}_{1} + \boldsymbol{B}_{1}\boldsymbol{B}_{0}}{\mu_{0}}\right] \hat{\boldsymbol{I}} \\
+ \left(P + \frac{\boldsymbol{B}_{1}^{2}}{2\mu_{0}} + \frac{\boldsymbol{B}_{1} \cdot \boldsymbol{B}_{0}}{\mu_{0}}\right) \hat{\boldsymbol{I}} \right] \\
= -\frac{\boldsymbol{B}_{1}}{\mu_{0}} [\overline{\nabla} \cdot (\boldsymbol{B}_{1} + \boldsymbol{B}_{0})] \\
- \frac{\boldsymbol{B}_{0}}{\mu_{0}} (\overline{\nabla} \cdot \boldsymbol{B}_{1}) - \frac{1}{\mu_{0}} [\overline{\nabla} \times \boldsymbol{B}_{0}] \times \boldsymbol{B}_{1}, \tag{4b}$$

$$\partial_{t} \left(\frac{\rho\boldsymbol{u}^{2}}{2} + \frac{P}{\gamma - 1} + \frac{\boldsymbol{B}_{1}^{2}}{2\mu_{0}}\right) \\
+ \overline{\nabla} \cdot \left[\left(\frac{\rho\boldsymbol{u}^{2}}{2} + \frac{\gamma P}{\gamma - 1}\right)\boldsymbol{u}\right] \\
+ \overline{\nabla} \cdot \left[\frac{[\boldsymbol{u}(\boldsymbol{B}_{1} + \boldsymbol{B}_{0}) - (\boldsymbol{B}_{0} + \boldsymbol{B}_{1})\boldsymbol{u}] \cdot \boldsymbol{B}_{1}}{\mu_{0}}\right] \\
= -\frac{(\boldsymbol{u} \cdot \boldsymbol{B}_{1})}{\mu_{0}} [\overline{\nabla} \cdot (\boldsymbol{B}_{1} + \boldsymbol{B}_{0})]. \tag{4c}$$

An advantage of splitting the magnetic field is that there are no quadratic terms in B_0 in Equation 4(b). Near the Sun (especially near active regions) such terms can be so large that the error in their approximation might exceed the whole

physical effect from the B_1 field. For the same reason we cannot, in general, rely on the assumption that numerical approximations for $\nabla \times B_0$ and $\nabla \cdot B_0$ are exactly zero (as it is theoretically assumed), so that to maintain entropy conservation we need to introduce the corresponding source terms in Equations 4(a)–(c). Particularly, all contributions from the field to the momentum Equation 4(b) can be combined with the Ampère force $j \times (B_1 + B_0) = \frac{1}{\mu_0} [\nabla \times B_1] \times (B_1 + B_0)$ and it is the last term in the RHS of Equation 4(b), which ensures that the potential, B_0 , contributes to the total field, but not to the current, in the Ampère force.

In a solar corona model different approximations, with split and non-split magnetic fields, can be used depending on the heliocentric distance, R = |R|. For instance, the "threaded field line model" Sokolov et al. (2021a), that includes the transition region and covers heliocentric distances between the photosphere (R_{\odot}) and the low boundary of the solar corona, $R_b \approx 1.1~R_{\odot}$, neglects the nonpotential B_1 component, assuming that in this region $B_1 \equiv 0$, and the plasma flow occurs only along the potential field lines (threads). This approach allows us to move the boundary conditions for all other physical quantities from the top of the transition region (where they are poorly known) to the photosphere. Accordingly, the boundary condition, $(B_1)_R = 0$, is imposed at $R = R_b$, to solve the full set of Equations 4(a)–(c) at distances $R_b \leqslant R \leqslant R_{SS}$.

Finally, above the magnetogram source surface, at $R \ge R_{SS}$, the B_0 field, which is purely radial at R_{SS} , can be naturally continued beyond the source surface as a steady state, radial, and divergence-free field decaying as $1/R^2$:

$$\boldsymbol{B}_0(\boldsymbol{R}) = \frac{R_{\rm SS}^2}{R^2} \boldsymbol{B}_0 \left(\frac{R_{\rm SS}}{R} \boldsymbol{R} \right). \tag{5}$$

This magnetic field, however, is no longer a potential field, therefore its contribution to the current cannot be neglected. To fully account for the total force effect when using split fields and to ensure their continuity at $R_{\rm SS}$, one needs to add the extra source term to the RHS of the momentum Equation 4(b) in the $R \geqslant R_{\rm SS}$ region:

$$S_{\mathbf{M}} = \frac{1}{\mu_0} \overline{\nabla} \cdot (\mathbf{B}_0 \mathbf{B}_0) - \frac{1}{2\mu_0} \overline{\nabla} \mathbf{B}_0^2 - \frac{1}{\mu_0} \mathbf{B}_0 (\overline{\nabla} \cdot \mathbf{B}_0) + \frac{1}{\mu_0} [\overline{\nabla} \times \mathbf{B}_0] \times \mathbf{B}_1, \tag{6}$$

which is easy to compute, since only the last term (which is to cancel the last term in the RHS of Equation 4(b)) depends on time via B_1 , while all other terms are steady-state terms and can be calculated only once.

With the newly added source, the momentum equation in effect reduces to Equation 1(c) expressed in terms of the total magnetic field, $\mathbf{B} = \mathbf{B}_0 + \mathbf{B}_1$, and the induction (Equation 4(a)) reduces to Equation 1(b). Nevertheless, it is the unknown field \mathbf{B}_1 that is solved from these equations throughout the computational domain. In order not to break the entropy conservation, for $R \geqslant R_{\rm SS}$ the corresponding source term, $S_E = \mathbf{u} \cdot \mathbf{S}_{\rm M}$, should be added to the RHS of the energy Equation 4(c). For derivations, but not for computations, the

RHS of the resulting energy equation can be written as follows:

$$u \cdot S_{M} - \frac{(u \cdot B_{1})}{\mu_{0}} [\overline{\nabla} \cdot (B_{1} + B_{0})]$$

$$= -\frac{[u \cdot (B_{1} + B_{0})]}{\mu_{0}} [\overline{\nabla} \cdot (B_{1}B_{0})]$$

$$+ \frac{1}{\mu_{0}} \overline{\nabla} \cdot \{ [(B_{1} + B_{0})u - u(B_{1} + B_{0})] \cdot B_{0} \}$$

$$- \frac{1}{\mu_{0}} B_{0} \cdot \partial_{t} B_{1}. \tag{7}$$

Although the energy Equation 4(c) with the split field and the transformed RHS is formally reducible to Equation 1(d) for the full field, such reduction would require us to redefine the magnetic energy density in terms of the total field too, as $(\mathbf{B}_1 + \mathbf{B}_0)^2/(2\mu_0)$, so that its time derivative, $(1/\mu_0)(\mathbf{B}_1 + \mathbf{B}_0) \cdot \partial_t \mathbf{B}_1$, balances the last term in the RHS of Equation (7). This redefinition, however, may compromise the whole idea of only solving equations for \mathbf{B}_1 beyond R_{SS} . To use the energy Equation 4(c), with an extra source, $\mathbf{u} \cdot \mathbf{S}_{M}$, seems to be a better option.

3. Reduced Equations of SA-MHD

3.1. Intuitive Solution

Now, we show how to proceed from standard MHD Equations 1(a)–(d) to equations for SA-MHD, in which

$$\mathbf{B} = \alpha \mathbf{u}, \qquad \mathbf{E} = -\mathbf{u} \times \mathbf{B} \equiv 0,$$
 (8)

where $\alpha(t, \mathbf{R})$ is a scalar function of time and coordinates. To derive a governing equation for α , in a steady-state streamaligned solution, one can integrate the MHD equations over a magnetic flux tube element of a length of $d\ell$ bounded by two nearby cross sections of the flux tube, dS_1 and dS_2 , and a bundle of magnetic field lines about a chosen magnetic field line, which all pass through the contours of these cross sections. The equation, $\overline{\nabla} \cdot \mathbf{B} = 0$, gives

$$BdS = const$$
 (9)

along the flux tube, which allows us to relate the change in the cross-section area along the thread to the magnetic field magnitude. Now, since the streamlines are aligned with the magnetic field lines, one can also integrate the continuity Equation 1(a) for a steady-state flow along the flux tube, which gives

$$\rho uS = \text{const} \tag{10}$$

Therefore, the ratio of constant mass flux and the constant magnetic flux,

$$\frac{B}{\rho u} \equiv \frac{\alpha}{\rho} \tag{11}$$

is constant along the field line and along the streamline. Both of these relations can be expressed as

$$(\boldsymbol{u} \cdot \overline{\nabla}) \frac{\alpha}{\rho} = 0 \tag{12}$$

Now, if we assume that this ratio is constant along the fluid particle trajectory (which in steady state coincides with the streamline but in the dynamic system this statement is a matter of a model assumption):

$$\partial_t \left(\frac{\alpha}{\rho} \right) + (\mathbf{u} \cdot \overline{\nabla}) \left(\frac{\alpha}{\rho} \right) = 0, \tag{13}$$

we can combine Equations 1(a) and (13) to obtain the conservation law for α :

$$\partial_t \alpha = -\overline{\nabla} \cdot (\alpha \mathbf{u}). \tag{14}$$

3.2. Rigorous Solution

A less intuitive but mathematically more rigorous derivation of the same set of model equations can be obtained if we consider an MHD state that is close to the force equilibrium, $\partial_t \mathbf{u} \to 0$, and add the aligning source (that tends to zero) to the induction equation (Equation 1(b)):

$$\partial_t \mathbf{B} + \overline{\nabla} \cdot (\mathbf{u}\mathbf{B} - \mathbf{B}\mathbf{u})$$

$$= -\mathbf{u}(\overline{\nabla} \cdot \mathbf{B}) + \alpha \partial_t \mathbf{u}, \qquad \alpha = \frac{\mathbf{B} \cdot \mathbf{u}}{\mathbf{u}^2}, \tag{15}$$

where the definition of α from Equation (8) is generalized for the case of nonaligned vectors \boldsymbol{u} and \boldsymbol{B} ; for the aligned vectors, both definitions are identical. To keep the entropy conservation, a similar source should be added to the RHS of the energy (Equation 1(d)):

$$\partial_{t} \left(\frac{\rho \mathbf{u}^{2}}{2} + \frac{P}{\gamma - 1} + \frac{\mathbf{B}^{2}}{2\mu_{0}} \right)$$

$$+ \overline{\nabla} \cdot \left[\left(\frac{\rho \mathbf{u}^{2}}{2} + \frac{\gamma P}{\gamma - 1} \right) \mathbf{u} \right]$$

$$+ \overline{\nabla} \cdot \left[\frac{\mathbf{B}^{2} \mathbf{u} - \mathbf{B} (\mathbf{u} \cdot \mathbf{B})}{\mu_{0}} \right]$$

$$= -\frac{(\mathbf{u} \cdot \mathbf{B})}{\mu_{0}} (\overline{\nabla} \cdot \mathbf{B}) + \frac{\alpha}{\mu_{0}} \mathbf{B} \cdot \partial_{t} \mathbf{u}$$
(16)

Now, if in an arbitrary MHD initial state the magnetic field is aligned according to Equation (8), the aligning term ensures that

$$\partial_t \mathbf{E} = [\partial_t \mathbf{B} \times \mathbf{u}] - [\partial_t \mathbf{u} \times \mathbf{B}]$$

= $[\partial_t \mathbf{u} \times (\alpha \mathbf{u} - \mathbf{B})] = 0,$ (17)

and keeps the alignment forever. By substituting $\mathbf{B} = \alpha \mathbf{u}$ into Equation (15), we arrive at Equation (14) (multiplied by \mathbf{u}).

In the momentum equation the stream-aligned magnetic field should be applied:

$$\partial_{t}(\rho \boldsymbol{u}) + \overline{\nabla} \cdot \left[\rho \boldsymbol{u} \boldsymbol{u} + P \hat{\boldsymbol{I}} - \frac{\alpha^{2}}{\mu_{0}} \left(\boldsymbol{u} \boldsymbol{u} - \frac{u^{2}}{2} \hat{\boldsymbol{I}} \right) \right]$$

$$= -\frac{\alpha}{\mu_{0}} \boldsymbol{u} \overline{\nabla} \cdot (\alpha \boldsymbol{u}), \tag{18}$$

which can be also written in a nonconservative form:

$$\partial_t \boldsymbol{u} + (\boldsymbol{u} \cdot \overline{\nabla}) \boldsymbol{u} = -\frac{\overline{\nabla}P}{\rho} + \frac{\alpha}{\mu_0 \rho} [\overline{\nabla} \times (\alpha \boldsymbol{u})] \times \boldsymbol{u}$$
 (19)

Equation (19) contains the explicit expression for the Ampère force, which happens to be always perpendicular to the velocity

vector (similarly to the Coriolis force). In the equation of energy Equation 1(d) the Poynting flux, $E \times B$ vanishes identically. In addition, the sources in the RHS of Equation (16) for the stream-aligned field reduce to $\partial_t B^2/2\mu_0$ and entirely balance the change in the magnetic energy density in the LHS. Therefore in effect, the stream-aligned magnetic field does not contribute to the energy density, so that the energy equation does not include the magnetic field at all:

$$\partial_t \left(\frac{\rho u^2}{2} + \frac{P}{\gamma - 1} \right) + \overline{\nabla} \cdot \left[\left(\frac{\rho u^2}{2} + \frac{\gamma P}{\gamma - 1} \right) \boldsymbol{u} \right] = 0. \quad (20)$$

This is because the Ampère force is perpendicular to the velocity vector and it does not affect the kinetic energy, hence, does not exchange energy between the field and plasma. For the same reason, under steady-state conditions, Equation (20) conserves the Bernoulli integral along the streamline in its classical form:

$$(\boldsymbol{u} \cdot \overline{\nabla}) \left[\frac{u^2}{2} + \frac{\gamma P}{(\gamma - 1)\rho} \right] = 0. \tag{21}$$

Equations 1(a), (14), (18), and (20) present a full set of governing equations which, as the solution approaches steady state, becomes fully conservative (the nonconservative source term that is proportional to $\partial_t \alpha$ in the momentum equation tends to zero), satisfies the $\overline{\nabla} \cdot \mathbf{B} = 0$, constrain (since $\overline{\nabla} \cdot \mathbf{B} = -\partial_t \alpha \to 0$), and their solution in this limit presents a legitimate solution of the MHD equations since the aligning sources $(\propto \partial_t \mathbf{u} \to 0)$ tend to zero too. Moreover, this is a desired stream-aligned solution. On the other hand the full MHD equations, with no aligning sources and once applied to any nonequilibrium MHD state, with $\partial_{\mu} \mathbf{u} \neq 0$, will immediately produce a non-stream-aligned solution even from a streamaligned initial state. It seems that in any discretized implementation (actual numerical solution) it is extremely difficult (if not impossible) to reach stream-aligned steady-state 3D solutions within the framework of regular computational MHD, which justifies the approach proposed here.

3.3. Stream-aligned MHD in a Rotating Frame of Reference

For applications to solar wind, the momentum and energy equations of SA-MHD are used the frame of reference rotating with angular velocity, Ω_{\odot} , with respect to the inertial frame. In addition to the Coriolis force density, $-2\rho\Omega_{\odot}\times u$, the centrifugal and gravitational forces are accounted for via the gradient of the potential, $\Phi(R)$:

$$\Phi(\mathbf{R}) = -\frac{GM_{\odot}}{R} - \frac{1}{2} [\mathbf{\Omega}_{\odot} \times \mathbf{R}]^2, \qquad (22)$$

$$\partial_{t}(\rho \mathbf{u}) + \overline{\nabla} \cdot \left[\rho \mathbf{u} \mathbf{u} + P \hat{\mathbf{I}} - \frac{\alpha^{2}}{\mu_{0}} \left(\mathbf{u} \mathbf{u} - \frac{\mathbf{u}^{2}}{2} \hat{\mathbf{I}} \right) \right]$$

$$= -\frac{\alpha}{\mu_{0}} \mathbf{u} \overline{\nabla} \cdot (\alpha \mathbf{u}) - 2\rho \Omega_{\odot} \times \mathbf{u} - \rho \overline{\nabla} \Phi, \qquad (23)$$

$$\partial_{t} \left[\rho \left(\frac{u^{2}}{2} + \Phi \right) + \frac{P}{\gamma - 1} \right] + \overline{\nabla} \cdot \left\{ \left[\rho \left(\frac{u^{2}}{2} + \Phi \right) + \frac{\gamma P}{\gamma - 1} \right] \boldsymbol{u} \right\} = 0.$$
 (24)

In the rotating frame the Bernoulli integral (Equation (21)) is modified by the inertial force potential (Equation (22)):

$$(\mathbf{u} \cdot \overline{\nabla}) \left[\frac{u^2}{2} - \frac{GM_{\odot}}{R} - \frac{1}{2} [\mathbf{\Omega}_{\odot} \times \mathbf{R}]^2 + \frac{\gamma P}{(\gamma - 1)\rho} \right] = 0.$$
(25)

The Bernoulli integral can be used to relate the model predictions at the source surface close to the Sun, such as the WSA predictions at $R = 2.5 R_{\odot}$, to the observed solar wind parameters at 1 au (see, e.g., Cohen et al. 2007). However, Equation (25) is not convenient for use, since the velocity in the inertial frame, u_{inert} , relates to that in the rotating frame, u, with the well-known equation:

$$u_{\text{inert}} = u + \Omega_{\odot} \times R,$$
 (26)

so that at 1 au the velocity in the rotating frame has a too-large contribution from rotational velocity. In terms of the observable parameters in the inertial frame, the Bernoulli integral implies the conservation of the following quantity:

$$\frac{u_{\text{inert}}^2}{2} - \Omega_{\odot} \cdot [\mathbf{R} \times \mathbf{u}_{\text{inert}}] - \frac{GM_{\odot}}{R} + h = \text{const}, \qquad h = \frac{\gamma P}{(\gamma - 1)\rho}. \tag{27}$$

Within the framework of isothermal approximation for solar atmosphere, one can use generic expression enthalpy per unit of mass, h, instead of a particular model for an ideal gas with constant γ assumed in Equation (27). For isothermal two-component plasma with $T_i = T_e = T$, the expression for enthalpy is $h = \frac{2k_BT}{m_p}\log\rho$. Note, that in neglecting the effect from the gas-kinetic

Note, that in neglecting the effect from the gas-kinetic pressure and from the magnetic field, for a test particle of a unit mass comoving with the solar stream velocity, \boldsymbol{u} , both the energy integral, $\frac{u_{\text{inert}}^2}{2} - \frac{GM_{\odot}}{R} = \text{const}$, and the vector of particle angular momentum, $[\boldsymbol{R} \times \boldsymbol{u}_{\text{inert}}] = \text{const}$, conserve separately, and so does their linear combination in Equation (27). However, the force effect of the stream-aligned magnetic field increases the angular momentum of the solar wind while moving outward from the Sun. Therefore, according to Equation (27), at large heliocentric distances there is a finite gain in the solar wind energy per unit of mass equal to $\Omega_{\odot} \cdot [\boldsymbol{R} \times \boldsymbol{u}_{\text{inert}}]_{l}$ au.

The closed system of equations describing the self-consistent variation of the angular momentum and azimuthal magnetic field component, while the solar wind propagating outward the Sun Parker (1958), can be obtained by solving the equations of SA-MHD in spherical coordinates, R, θ , φ , which are the heliocentric distance, colatitude, and longitude, respectively. The analytical solution may be found assuming no dependence on φ (axially symmetric field) and no motion over θ (radially divergent flow). The Coriolis force forces the particles to rotate in the negative φ direction, while it has no component in the θ direction. Consequently, the fluid motion occurs only in the (R, φ) direction, and all streamlines will be on conical surfaces of constant θ . Steady-state stream-aligned solutions of Equations 1(a), (23), (24) may be integrated along streamlines yielding

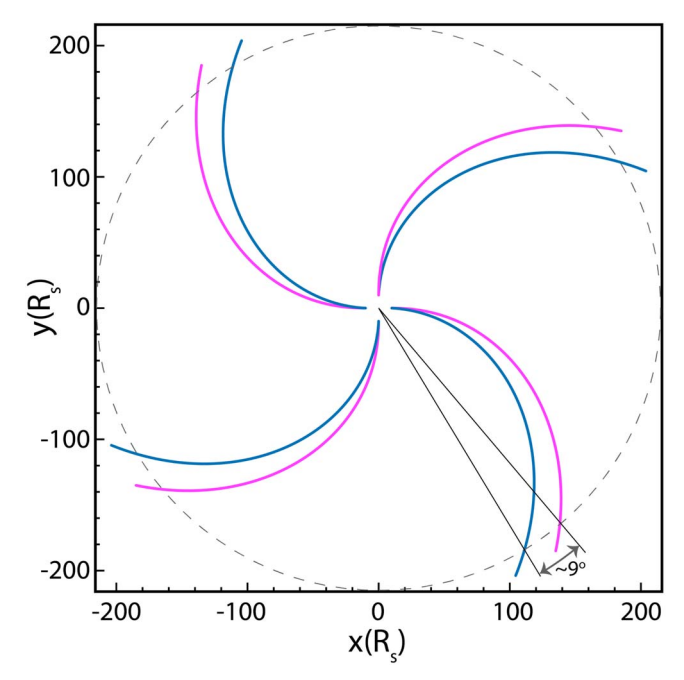


Figure 1. Parker (1958) solutions (magenta) vs. the SA-MHD solution by Weber & Davis (1967) (blue) in the equatorial plane for a uniform solar corona. A constant solar wind speed of $u_R = 400 \text{ km s}^{-1}$ and source surface radius of $10 R_{\odot}$ are assumed.

the following equation:

$$R\sin\theta \left[\left(1 - \frac{\alpha^2}{\mu_0 \rho} \right) u_{\varphi} + \Omega_{\odot} R \sin\theta \right]$$
$$= \cos\theta = \Omega_{\odot} \sin^2\theta \left\{ R^2 \right\}_{A}. \tag{28}$$

In the absence of the magnetic field, i.e., at $\alpha \equiv 0$, Equation (28) would express the conservation of angular momentum $(R \sin \theta u_{\varphi, \text{inert}} \equiv |\mathbf{R} \times \mathbf{u}_{\text{inert}}|)$ in the inertial (not rotating) system. However, due to the effect from the realistic interplanetary magnetic field, the heliocentric distance on the right-hand side should be taken at the Alfvén point where the local stream speed, u, equals to the Alfvén wave speed, $V_{\rm A} = B/\sqrt{\mu_0 \rho}$, since

$$\frac{\alpha^2}{\mu_0 \rho} = \frac{V_A^2}{u^2} = \frac{1}{M_A^2}.$$
 (29)

Typically, the factor M_A^{-2} is very large near the base of the solar corona, because in this region the solar magnetic field is large and the solar wind is not accelerated yet. In the opposite limiting case at large heliocentric distances, where the solar wind is fast and the magnetic field is weak, the plasma stream is hyperalfvénic, M_A^{-2} is negligibly small. In between the accelerating and rarefying solar wind must go through the Alfvén point and this is the point at which the integration constant is determined (this point to avoid discontinuous solutions). With these considerations the azimuthal velocity is (see Weber & Davis 1967):

$$u_{\varphi} = \frac{\Omega_{\odot} \sin \theta \left[(R^2)_{\mathcal{A}} - R^2 \right]}{R \left(1 - \frac{1}{M_{\mathcal{A}}^2} \right)}.$$
 (30)

Figure 1 demonstrates the difference between the oversimplified Parker (1958) spiral and the SA-MHD solution

according to Equation (30). One can see that under idealized conditions (constant solar wind speed of $u_R = 400 \text{ km s}^{-1}$ and source surface radius of $10\,R_\odot$) the more accurate streamaligned solution Equation (30) lags behind the Parker (1958) spiral by about 9° at Earth's orbit. Taking into account the solar rotation (with respect to Earth) this means that a stream-aligned field line originating from the same point of the solar surface will cross Earth about 15 hr later than the corresponding Parker (1958) spiral aligned field line. In space weather applications, tracing the streamline in the corotating frame from the observation point toward its origin site can be used to associate in situ solar wind properties to remotely observed structures of the solar corona (see, e.g., Biondo et al. 2021). The large difference demonstrated in Figure 1 means that field line associated phenomena (like SEP events) will arrive at Earth some 15 hr later than predicted by simple Parker (1958) spiral connectivity models. It is, therefore, important that our computational model fully incorporates all principles and capabilities of earlier models.

4. Simulation Results and Discussion

4.1. Numerical Solution with Full MHD

For comparison with the SA-MHD numerical result presented later in this paper, we provide a numerical solution for the steady-state solar corona prior to the SEP event that occurred on 2013 April 11 (Lario et al. 2014). GONG magnetogram at 2013 April 11, 06:04 UT serves as the inner boundary condition and the main driver of the solar wind model (see the left panel of Figure 2).

In the simulation, the initial condition of the 3D magnetic fields in the solar corona is reconstructed by a potential field source surface (PFSS) solution using a spherical harmonic expansion with the inner boundary provided by the magnetogram. The radial magnetic fields on the surface of the Sun calculated using PFSS is shown in the right panel of Figure 2. The PFSS reconstruction has been used to obtain the potential (\mathbf{B}_0) field below the source surface located at 2.5 R_{\odot} . Below the source surface we solve the full set of MHD Equations 1(a) and (4a)-(c), above it we add the source term $S_{\rm M}$ given by Equation (6) to the momentum equation, (Equation 4(b)), as well as the extra energy source, $u \cdot S_{M}$, to the energy equation, (Equation 4(c)). The governing equations for the solar corona and inner heliosphere models described by Sokolov et al. (2021a) are solved using the SWMF (Tóth et al. 2005; Toth et al. 2012) developed at the University of Michigan.

The magnetic field in the equatorial plane (Figure 3 top panels) and in the y=0 meridional plane of the rotating HGR coordinate system (Figure 3 bottom panels) exhibits visible imperfections in the form of disconnected ("V-shaped") field lines below $20\,R_\odot$ and too long closed loops in (the middle bottom panel of Figure 3). The magnetic field in the equatorial plane of the inner heliosphere (right panels in Figure 3) is totally disordered and is not applicable to solving magnetic connectivity. We emphasize that this feature is independent of the numerical solution algorithm: while steady-state field lines and streamlines are identical at the PDE level, this is not true in any discretization within the framework of computational MHD. The stream-aligned model is designed to address all these issues.

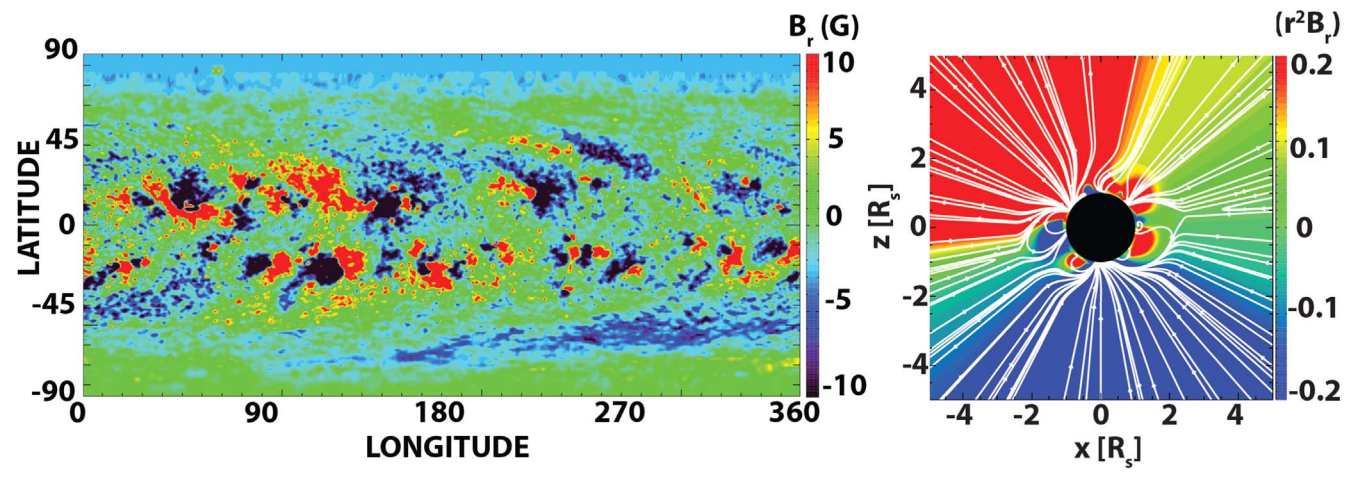


Figure 2. Left: Radial magnetic field from GONG magnetogram observation at 2013 April 11, 06:04 UT. Right: Radial magnetic field calculated using PFSS Model with spherical harmonics of order 90. Simulations with 180 harmonics were less stable.

4.2. The Leontovich Boundary Condition as the Aligning Source

The computational SA-MHD cannot be applied to the entire solar corona that starts with a slowly expanding atmosphere with speeds as low as a few km/s on top of the transition region and in closed field regions. The slow-speed region extends to heliocentric distances of 2.5– $3.5\,R_{\odot}$. In this region the SA-MHD would fail to describe closed magnetic field lines. In addition, the problem to align the strong magnetic field with the slow and somewhat random motion is not only physically inappropriate but also mathematically ill-posed, since the characteristic perturbation speeds tend to infinity if the plasma speed tends to zero. Therefore, we successfully apply the SA-MHD above some spherical heliocentric boundaries with a radius of $R_{\rm SA}$.

Below this boundary we apply source terms in the MHD equation, which are proportional to the electric field describing the nonalignment between the field and flow and turning to zero when the alignment is achieved. These terms reduce the electric field below $R_{\rm SA}$ and entirely eliminate it at $R=R_{\rm SA}$. However, they do not prevent slow motions and magnetic field line reconnection and closure. The sources are heuristically derived from the well-known Leontovich (1948) boundary condition which makes them physics-based.

The Leontovich boundary condition (Leontovich 1948; Landau et al. 1985) is applicable to electromagnetic fields when a high-frequency wave interacts with a metal, and deep inside the metal, the field vanishes. The currents shielding the field are assumed to be concentrated in a thin layer near the boundary, having the impedance, Z. Under these assumptions the transverse components of electric and magnetic fields outside the metal are related to boundary condition:

$$\boldsymbol{E}_{t} = Z \; \boldsymbol{B}_{t} \times \hat{\boldsymbol{n}}, \tag{31}$$

where \hat{n} is a unit vector normal to the metal surface directed inward the metal. A straightforward (however, insufficient) application to the boundary between the usual and SA-MHD gives us an opportunity to consider the electric field-free SA-MHD region as if this is the metal and to assign the impedance Z to the boundary surface. In this case at the MHD side of this boundary the finite electric field will cause a change in the B_0

field given by Equation (31):

$$\delta \mathbf{B}_0 = \hat{\mathbf{n}} \times \mathbf{E}/\mathbf{Z},\tag{32}$$

It is important to emphasize that this field is induced by the current which is not conducted by the moving solar wind plasma, that is why Equation (32) describes B_0 field, rather than B_1 . Another comment is that the field undergoes a jump across the surface at which the finite current is concentrated, that is why the field given by Equation (32) exists only "outside the metal," that is in the SA-MHD region that starts at a heliocentric distance of $R = R_{SA}$. The modified field contributes to the flux function resulting in the evolution of the MHD state toward higher alignment (lower electric field). The effect is easy to evaluate if the impedance surface is orthogonal to the magnetic field. In this case the electric field $E = B_n \hat{\mathbf{n}} \times \mathbf{u}_t$ is orthogonal to \hat{n} . The normal components, $B_n = \mathbf{B} \cdot \hat{n}$, $u_n = \mathbf{u} \cdot \hat{\mathbf{n}}$ of the field and velocity are not affected by the extra field given by Equation (32), while the transverse velocity and field in the layer of a thickness of Δx , orthogonal to the magnetic field evolve since the extra field Equation (32) is present at the upper boundary of the slab and absent at the lower one. Using the flux functions in Equations 4(a), (b), one can find the source terms for the MHD velocity, $(\partial_t \mathbf{u})_L$, and for the induction field, $(\partial_t \mathbf{B})_L$, caused by the shielding currents implied in the Leontovich (1948) boundary condition (that is why we use subscript L):

$$(\partial_t \mathbf{u})_L = \frac{B_n \delta \mathbf{B}_0}{\rho \Delta x \mu_0} = -\frac{V_A^2 \mathbf{u}_t}{Z \Delta x} \tag{33}$$

$$(\partial_t \mathbf{B})_L = -\frac{u_n \delta \mathbf{B}_0}{\Delta x} = \frac{B_n u_n \mathbf{u}_t}{Z \Delta x},\tag{34}$$

in the last equation one can also put $B_n u_n = \mathbf{B} \cdot \mathbf{u}$, since the normal vector is aligned with the field, hence, $\mathbf{B} = B_n \hat{\mathbf{n}}$. Now, one can derive aligning sources assuming the distributing conducting layers instead of concentrated impedance by substituting d(1/Z)/dx for $1/(Z\Delta x)$ ratio, which may be conveniently parameterized as $d(1/Z)/dx = 1/(V_A^2 + u_n^2)\tau$, so that:

$$(\partial_t \mathbf{u})_L = -\frac{V_A^2 \mathbf{u}_t}{(V_A^2 + u_n^2)\tau} \tag{35}$$

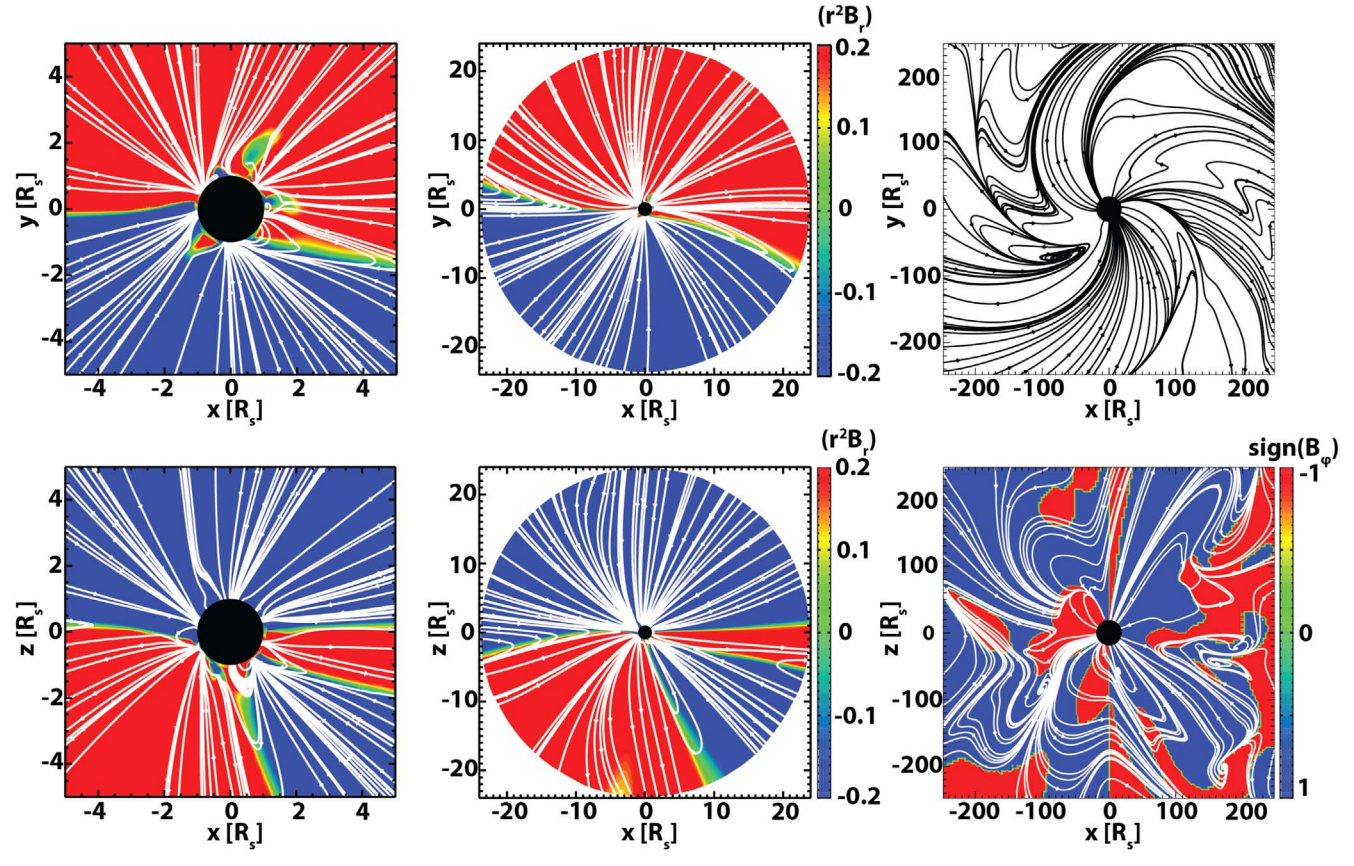


Figure 3. The magnetic field in the equatorial plane (top panels) and in the y = 0 meridional planes (bottom panels) of the rotating HGR coordinate system.

$$(\partial_t \mathbf{B})_L = \frac{(\mathbf{B} \cdot \mathbf{u})\mathbf{u}_t}{(V_A^2 + u_n^2)\tau}.$$
 (36)

These sources at some choice of τ can be added to the MHD equations in a chosen region, not necessarily near the boundary. The advantage of the chosen parameterization is that τ directly characterizes the electric field relaxation due to the aligning sources, since:

$$(\partial_t \mathbf{E})_L = B_n \hat{\mathbf{n}} \times (\partial_t \mathbf{u})_L - u_n \hat{\mathbf{n}} \times (\partial_t \mathbf{B})_L = -\frac{\mathbf{E}}{\tau}.$$
 (37)

Although greatly improving the MHD solution at $R < R_{\rm SA}$, the source terms do not allow us to align the solution at $R \to R_{\rm SA}$. The latter goal is achieved if while integrating numerically the MHD equations over time after advancing the solution through the time step, Δt , we add the source terms and assume that the relaxation rate, $1/\tau$, is equal to $1/\Delta t$ at $R \to R_{\rm SA}$ and modulated with some geometric factor, ξ , which equals one at $R \to R_{\rm SA}$ and decays at smaller heights. In other words, the linear aligning operator is applied to the velocity and magnetic field vectors in the following manner:

$$\boldsymbol{u} \to \boldsymbol{u} + \Delta \boldsymbol{u}_L, \qquad \Delta \boldsymbol{u}_L = -\frac{\xi V_A^2 \boldsymbol{u}_t}{V_A^2 + u_n^2}$$
 (38)

$$\mathbf{B} \to \mathbf{B} + \Delta \mathbf{B}_L, \qquad \Delta \mathbf{B}_L = \frac{\xi(\mathbf{B} \cdot \mathbf{u})\mathbf{u}_t}{V_A^2 + u_n^2}.$$
 (39)

The total energy density decreases by the following quantity:

$$\Delta \mathcal{E}_L = \frac{\left(\frac{\xi^2}{2} - \xi\right) V_A^2 \rho \boldsymbol{u}_t^2}{V_A^2 + u_n^2}.$$
 (40)

At $\xi = 1$, that is in the proximity of the SA-MHD computational domain, operator Equations (38), (39) provides a perfect alignment about some weighted average direction such that the weak field is aligned with the strong stream without noticeable modification in the stream direction and, in the opposite limiting case, slow flow is aligned with the strong field.

4.3. Numerical Solution with SA-MHD

The simulation results with SA-MHD are provided for the same solar configuration as described in Section 4.1. Below the PFSS source surface at $R=2.5\,R_\odot$ the MHD model is not modified and the numerical solution is not much different from that provided in Figure 2.

In the intermediate region $2.5\,R_\odot < R < 3.5\,R_\odot$ we apply the aligning operator Equations (38), (39) based on the Leontovich boundary condition as described in Section 4.2. The geometric factor $\xi = R/R_\odot - 2.5$ is chosen equal to zero at the lower boundary and one at the upper boundary, of this region.

At $R = R_{\rm SA} = 3.5\,R_{\odot}$ the MHD solution is enforced to be aligned so that above this boundary the SA-MHD equations are solved numerically. The characteristic perturbation speeds needed to construct the numerical scheme are discussed in the Appendix.

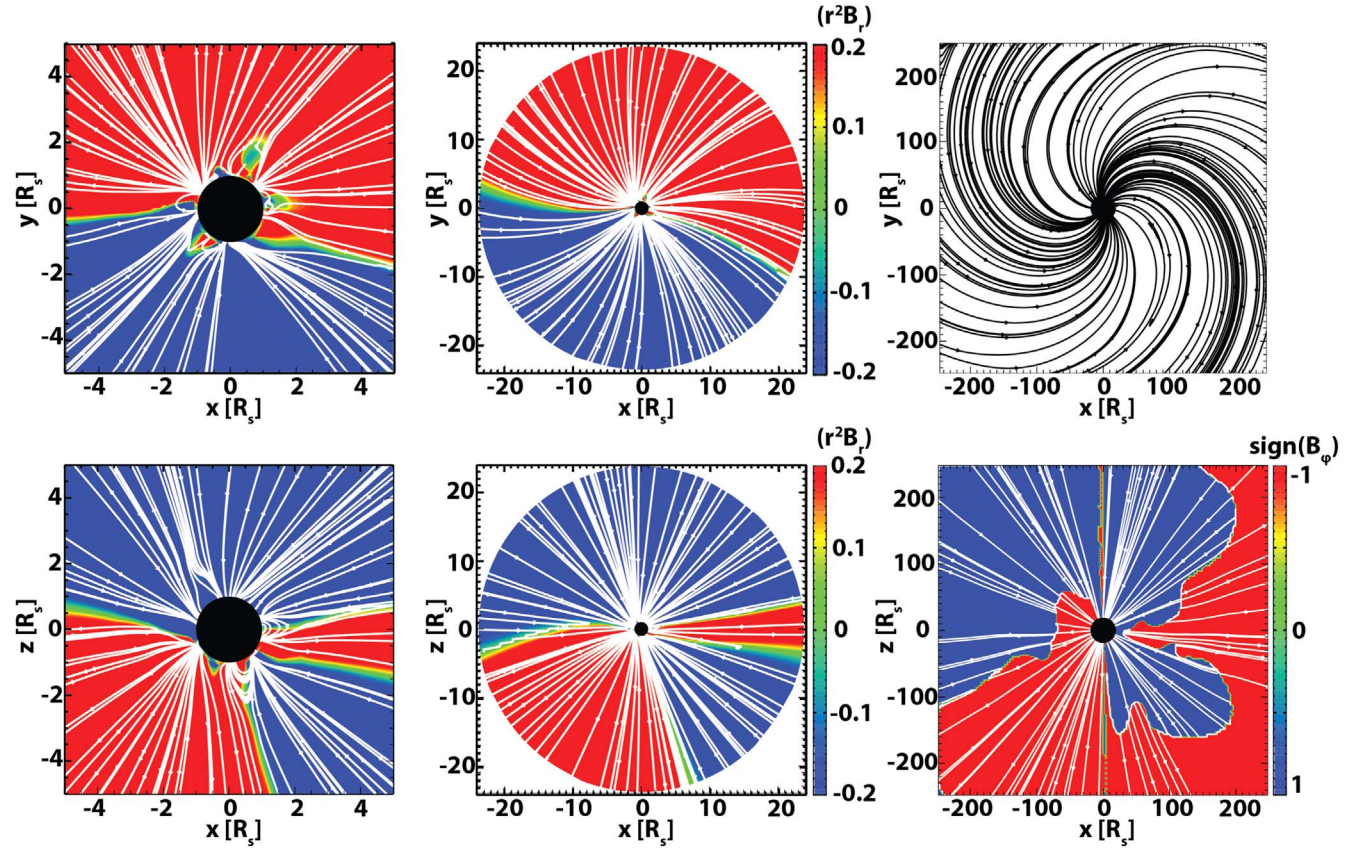


Figure 4. SA-MHD solutions of magnetic field lines in the equatorial plane of the inner heliosphere in the rotating HGR coordinate system.

Figure 4 shows the magnetic field structure in the corona and inner heliosphere obtained with SA-MHD and the Leontovich (1948) boundary condition. One can see that the unphysical features seen in Figure 3 are gone: There are no long closed loops or V-shaped field lines, and the magnetic field lines in the inner heliosphere clearly form a Parker (1958) spiral.

4.4. Magnetic Connectivity

Magnetic connectivity (the magnetic field line connecting a point of interest in the heliosphere to the solar photosphere) is a very important component of space weather simulations. Among other things magnetic connectivity controls the simulated intensity and time profiles of SEP events (see Borovikov et al. 2018; Li et al. 2021; Young et al. 2021).

For the synoptic map shown in Figure 2, the streamlines are not as simple as in the case of uniform solar wind speed (see Figure 1). As one sees in Figure 5, the delay between the Earth crossing of MHD and SA-MHD streamlines can vary between a few hours and a few days, depending on the actual angular radial speed profile.

Most existing SEP models use MHD streamlines as proxies for IMF lines and solve the SEP transport along these streamlines. Our results indicate that this approach should be used with great care: the Earth crossing of an interplanetary streamline can be off by a few hours or a few days depending on actual solar wind conditions. In addition, the sign of the radial magnetic field component can flip back and forth depending on the heliospheric current sheet crossings, so the $\mu = \cos(pitch - angle)$ quantity (appearing in the focused transport equation of Skilling 1971) might abruptly change the sign along the streamline. An equation

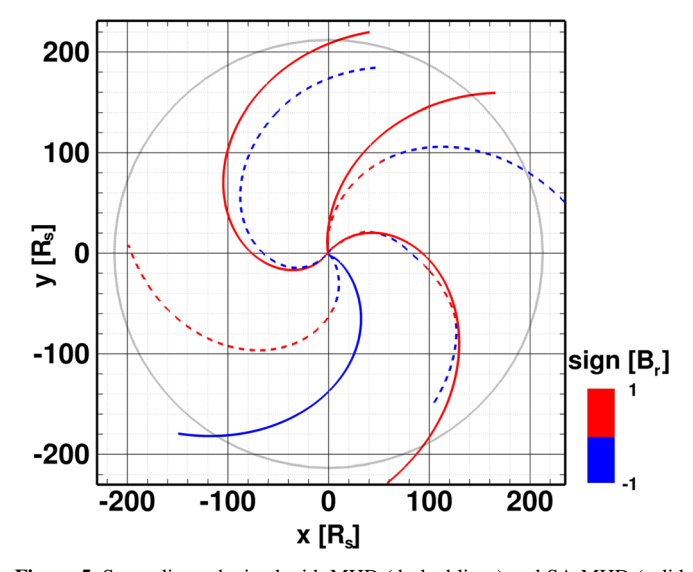


Figure 5. Streamlines obtained with MHD (dashed lines) and SA-MHD (solid lines). The streamlines are colored by the sign of the radial component of the local magnetic field vector. One can see that the sign of the radial magnetic field "flips" whenever the streamline crosses the heliospheric current sheet.

describing energetic particle transport in SA-MHD and a method to solve such equation numerically is described in a follow-up paper (Sokolov et al. 2021b).

5. Conclusion

We showed how the MHD equations can be modified to describe stream-aligned steady-state flows of plasma parallel to the magnetic fields with no electric field. We call this approach stream-aligned MHD (SA-MHD). We applied the new approach to modeling the solar corona and heliosphere in a coordinate frame corotating with the Sun. Domains using the SA-MHD approach can gradually be merged to regions in which the ordinary MHD equations are solved by distributed external currents similar to those implied by the Leontovich (1948) boundary condition. With this approach, the numerical solution in the heliosphere is perfectly aligned with the IMF lines shaped as classical Parker spirals. Our model addresses the magnetic connectivity problem as well as the simulation of the SEP acceleration and transport.

This work was supported by the NASA Heliophysics DRIVE Science Center (SOLSTICE) at the University of Michigan under grant NASA 80NSSC20K0600. We would also like to acknowledge high-performance computing support from (1) Yellowstone (ark:/85065/d7wd3xhc) provided by NCAR's Computational and Information Systems Laboratory, sponsored by the National Science Foundation, and (2) Pleiades operated by NASA's Advanced Supercomputing Division.

Appendix Characteristic Wave Speeds and Eigenvectors

In order to demonstrate an effect of the aligning terms on the characteristic waves, one can linearize Equations (15) and (16), together with Equations 1(a), (c). For linear characteristic perturbations, $(\delta\rho, \delta u, \delta P, \delta B)^T$, propagating along the x axis, i.e., depending on the coordinates and time via the combination, (x-Dt). The background for the wave propagation is (ρ_0, u_0, P_0, B_0) where $B_0 = (B_{x0}, B_{y0}, 0)$. The z component of the magnetic field is made zero by choosing a coordinate system in which the magnetic field vector is in the (x,y) plane. In the equations for the perturbation, all time derivatives should be substituted with $\partial_t = -D\partial_x$, and, after this substitution, one can omit the x derivatives by denoting $\partial_x(\delta\rho) \to \delta\rho$, etc. Note that De Sterck et al. (1999) analyzed eigenvalues of two-dimensional steady-state SA-MHD; however, such eigenvalues only characterize the direction of wave propagation rather than their speed needed to construct numerical schemes.

For the eight wave MHD with the aligning sources, the characteristic equations become:

$$-\Lambda \delta \rho + \rho_0 \delta u_x = 0, \tag{A1a}$$

$$-\Lambda \delta u_x + \frac{\delta P}{\rho_0} + \frac{B_{y0} \delta B_y}{\mu_0 \rho_0} = 0, \tag{A1b}$$

$$-\Lambda \delta u_y - \frac{B_{x0}\delta B_y}{\mu_0 \rho_0} = 0, \tag{A1c}$$

$$-\Lambda \delta u_z - \frac{B_{x0}\delta B_z}{\mu_0 \rho_0} = 0, \tag{A1d}$$

$$-\Lambda \delta P + \gamma P_0 \delta u_x = 0, \tag{A1e}$$

$$-\Lambda \delta B_{\rm r} + \alpha (\Lambda + u_{\rm r0}) \delta u_{\rm r} = 0, \tag{A1f}$$

$$-\Lambda \delta B_y + [\alpha \Lambda + (\alpha u_{x0} - B_{x0})] \delta u_y + B_{y0} \delta u_x = 0, \quad (A1g)$$

$$-\Lambda \delta B_z + [\alpha \Lambda + (\alpha u_{x0} - B_{x0})] \delta u_z = 0, \tag{A1h}$$

where $\Lambda = D - u_{x0}$ is the characteristic speed in the plasma frame.

Equations A1(a), (f) are independent and describe the propagation of two perturbations with the plasma speed $(D = u_{x0}, \Lambda = 0)$ in which

(W1):
$$\Lambda_1 = 0$$
, $\delta(\rho, u_x, u_y, u_z, P, B_x, B_y, B_z)^T$
= $(1, 0, 0, 0, 0, 0, 0, 0)^T \delta W_1$, (A2)

(W6):
$$\Lambda_6 = 0$$
, $\delta(\rho, u_x, u_y, u_z, P, B_x, B_y, B_z)^T$
= $(0, 0, 0, 0, 0, 1, 0, 0)^T \delta W_6$. (A3)

These are the entropy wave and the $\overline{\nabla} \cdot \boldsymbol{B}$ wave respectively (see Powell et al. 1999). Herewith, $\delta W_{1:8}$ denote arbitrary amplitudes of perturbations.

Equations A1(h), (d) can be solved separately:

$$\Lambda_{5,7} \delta u_z = -\frac{V_{A,x} \delta B_z}{\sqrt{\mu_0 \rho_0}}, \quad V_{A,x} = \frac{B_{x0}}{\sqrt{\mu_0 \rho_0}},
\tilde{V}_{A,x} = \frac{\alpha V_{A,x}}{\sqrt{\mu_0 \rho_0}},
\Lambda_{5,7} = -\frac{\tilde{V}_{A,x}}{2} \mp \sqrt{\frac{\tilde{V}_{A,x}^2}{4} + V_{A,x}^2 - u_{x0} \tilde{V}_{A,x}}, \quad (A4)$$

This pair of waves can be considered in two limiting cases. In the first limiting case we consider "traditional" MHD with no alignment source. Now one can put $\alpha=0$, $\tilde{V}_{A,x}=0$ in Equation (A4). Note that for $B_{x0}>0$ and $u_{x0}>0$ the perturbations of velocity and magnetic field are parallel in the left propagating wave ($\Lambda<0$), but they are antiparallel in the wave propagating to the right, creating or increasing field misalignments with the stream. Both of these Alfvén waves can exist in the absence of an aligning source and propagate with the Alfvén speed, $V_{A,x}=B_{x0}/\sqrt{\mu_0\rho_0}$.

The other limiting case is when we include the aligning source and assume a stream-aligned background ($B_{x0} = \alpha u_{x0}$). Under these circumstances, $V_{A,x}^2 = u_{x0} \tilde{V}_{A,x}$ and Equation (A4) describes two types of waves. In one of them, propagating to the left (upwind), the perturbation is stream aligned, $\delta B_z = \alpha \delta u_z$:

(W5):
$$\Lambda_5 = -\tilde{V}_{A,x}$$
,

$$\tilde{V}_{A,x} = \frac{\alpha^2 u_{x0}}{\mu_0 \rho_0} = \frac{u_{x0}}{M_A^2} = \frac{V_{A,x}}{M_A}$$
,
$$\delta(\rho, u_x, u_y, u_z, P, B_x, B_y, B_z)^{\mathrm{T}}$$

$$= (0, 0, 0, 1, 0, 0, 0, \alpha)^{\mathrm{T}} \delta W_5. \tag{A5}$$

This means that the left Alfvén wave still exists, but its characteristic speed adjusts ($\tilde{V}_{A,x} \neq V_{A,x}$ at $M_A \neq 1$) to ensure that the (parallel) perturbations of velocity and magnetic field are aligned. However, the right Alfvén wave in which the perturbations are antiparallel (and they cannot be aligned) is arrested: Equation (A4) requires the speed of this perturbation to be zero and the magnetic field to be unperturbed:

(W7):
$$\Lambda_7 = 0$$
, $\delta(\rho, u_x, u_y, u_z, P, B_x, B_y, B_z)^T$
= $(0, 0, 0, 1, 0, 0, 0, 0)^T \delta W_7$. (A6)

Analogously, Equations A1(g), (c) allow a wave propagating with the plasma:

(W8):
$$\Lambda_8 = 0$$
, $\delta(\rho, u_x, u_y, u_z, P, B_x, B_y, B_z)^T$
= $(0, 0, 1, 0, 0, 0, 0, 0)^T \delta W_8$. (A7)

Here, again, the perturbation speed is zero and the perturbations are not aligned. In the MHD description without the aligning sources, this would be the slow magnetosonic wave. We see that in MHD (two three-component-vector equations + two scalar equations, eight characteristic waves) with the aligning sources and stream-aligned background two kinds of waves (right Alfvén and right slow magnetosonic) degenerate. These are the only waves in which the perturbations are not stream aligned. The distinction of SA-MHD (one three-component-vector equation + three scalar equations with six characteristic waves) is that it lacks these two degenerate waves since this approximation does not allow nonaligned perturbations.

A1. Characteristic Waves in Stream-aligned MHD

Instead of three components of the magnetic field, we introduce a background value, α_0 , and linear perturbation, $\delta\alpha$, for the quantity, α , obeying the equation:

$$-\Lambda\delta\alpha + \alpha_0\delta u_x = 0. \tag{A8}$$

In the entropy wave (W1) and the modified Alfvén wave (W5) we have $\delta\alpha = 0$, while in the $\nabla \cdot \mathbf{B}$ wave (W6) the velocity perturbation should maintain the continuity of the stream-aligned field, $\delta\alpha u_{y0} + \alpha_0\delta u_y = 0$, so that $\delta(\rho, u_x, u_y, u_z, P, \alpha)^T = (0, 0, -u_{y0}, 0, 0, \alpha_0)^T \delta W_6$.

In the remaining three branches of waves, the magnetic field is stream aligned and there is a relationship between δu_y and δB_y :

$$\delta u_{y} = -\frac{\alpha_{0} u_{x0}}{\mu_{0} \rho_{0} \Lambda} \delta B_{y},$$

$$\times (\Lambda + \tilde{V}_{A,x}) \delta B_{y} - B_{y0} \delta u_{x} = 0. \tag{A9}$$

In the particular case of magnetic field-aligned propagation $(B_{y0} = 0)$ this reduces to the expression for another Alfvén wave of different polarization:

(W3a):
$$\Lambda_3 = -\tilde{V}_{A,x}, \quad \delta(\rho, u_x, u_y, u_z, P, \alpha)^T$$

= $(0,0, 1,0, 0,0)^T \delta W_2,$ (A10)

In the special case of $B_{y0} = 0$ Equations A1(b) and (e) give two sound waves:

(W2a) & (W4a):
$$\Lambda_{2,4} = \mp c_s$$
, $c_s^2 = \frac{\gamma P_0}{\rho_0}$,
 $\delta(\rho, u_x, u_y, u_z, P, \alpha)^{\mathrm{T}}$

$$= \left(\frac{\rho_0}{\Lambda_{2,4}}, 1, 0, 0, \frac{c_s^2 \rho_0}{\Lambda_{2,4}}, \frac{\alpha_0}{\Lambda_{2,4}}\right)^{\mathrm{T}} \delta W_{2,4}.$$
(A11)

In the general case when $B_{y0} \neq 0$ there are three wave branches, in which the perturbations of velocity, pressure, and magnetic

field are all interrelated:

$$(W2b), (W3b) & (W4b):$$

$$- \Lambda_{2:4} + \frac{c_s^2}{\Lambda_{2:4}} + \frac{V_{A,y}^2}{\Lambda_{2:4} + \tilde{V}_{A,x}} = 0, \quad V_{A,y}^2 = \frac{B_{y0}^2}{\mu_0 \rho_0},$$

$$\delta(\rho, u_x, u_y, u_z, P, \alpha)^{\mathrm{T}}$$

$$= \left(\frac{\rho_0}{\Lambda_{2:4}}, 1, -\frac{\tilde{V}_{A,x} u_{y0}}{\Lambda_{2:4}(\Lambda_{2:4} + \tilde{V}_{A,x})}, 0, \frac{c_s^2 \rho_0}{\Lambda_{2:4}}, \frac{\alpha_0}{\Lambda_{2:4}}\right)^{\mathrm{T}} \delta W_{2:4},$$
(A12)

This cubic equation always has three roots, corresponding to two fast and one slow magnetosonic wave. The characteristic speeds for $u_{0,x} > 0$ range (from most negative to largest positive) as: left fast magnetosonic, left Alfvén, left slow magnetosonic, combined entropy $+\overline{\nabla}\cdot \boldsymbol{B}$ wave, right fast magnetosonic wave. For $u_{0,x} < 0$ the order is reversed, with changing "left" to "right."

ORCID iDs

Igor V. Sokolov https://orcid.org/0000-0002-6118-0469 Lulu Zhao https://orcid.org/0000-0003-3936-5288 Tamas I. Gombosi https://orcid.org/0000-0001-9360-4951

References

Altschuler, M. D., Levine, R. H., Stix, M., & Harvey, J. 1977, SoPh, 51, 345

```
Arge, C. N., & Pizzo, V. J. 2000, JGR, 105, 465
Biondo, R., Bemporad, A., Mignone, A., & Reale, F. 2021, JSWSC, 11, 7
Borovikov, D., Sokolov, I. V., Roussev, I. I., Taktakishvili, A., &
   Gombosi, T. I. 2018, ApJ, 864, 88
Cohen, O., Sokolov, I. V., Roussev, I. I., et al. 2006, ApJL, 654, L163
Cohen, O., Sokolov, I. V., Roussev, I. I., et al. 2007, ApJL, 654, L163
Cranmer, S. R. 2010, ApJ, 710, 676
De Sterck, H., Low, B. C., & Poedts, S. 1999, PhPl, 6, 954
Dmitruk, P., Matthaeus, W. H., Milano, L. J., et al. 2002, ApJ, 575, 571
Godunov, S. K. 1961, Sov. Math. Dokl., 2, 947
Godunov, S. K. 1972, Numerical Methods for Mechanics of Continuum
  Medium, Vol. 1 (Novosibirsk: Siberian Branch of USSR Acad. of Sci.), 26
Gombosi, T., Chen, Y., Glocer, A., et al. 2021, JSWSC, 11, 41
Gombosi, T. I., Toth, G., De Zeeuw, D. L., et al. 2002, JCoPh, 177, 176
Gombosi, T. I., van der Holst, B., Manchester, W. B., & Sokolov, I. V. 2018,
   LRSP, 15, 4
Gosling, J. T. 1993, JGR, 98, 18937
Harten, A., Lax, P. D., & van Leer, B. 1983, SIAMR, 25, 35
Hu, Y. Q., Esser, R., & Habbal, S. R. 2000, JGR, 105, 5093
Landau, L. D., Lifshitz, E. M., & Pitaevskii, L. P. 1985, Electrodynamics of
   Continuous Media (2nd edn.; Oxford: Butterworth-Heinemann)
Lario, D., Raouafi, N. E., Zhang, J., Dresing, N., & Riley, P. 2014, ApJ, 797, 8
Leontovich, M. 1948, in Investigations on Propagation of Radio Waves, ed.
   B. Vvedenskii (Moscow: AN SSSR), 5
Li, G., Jin, M., Ding, Z., et al. 2021, ApJ, 919, 146
Li, X., & Habbal, S. R. 2003, ApJL, 598, L125
Lionello, R., Velli, M., Downs, C., Linker, J. A., & Mikić, Z. 2014a, ApJ,
   796, 111
Lionello, R., Velli, M., Downs, C., et al. 2014b, ApJ, 784, 120
Ogino, T., & Walker, R. J. 1984, GeoRL, 11, 1018
Oran, R., van der Holst, B., Landi, E., et al. 2013, ApJ, 778, 176
Osman, K. T., Matthaeus, W. H., Greco, A., & Servidio, S. 2011, ApJL,
  727, L11
Parker, E. N. 1958, ApJ, 128, 664
Pomoell, J., & Poedts, S. 2018, JSWSC, 8, A35
Powell, K., Roe, P., Linde, T., Gombosi, T., & De Zeeuw, D. L. 1999, JCoPh,
Roussev, I. I., Gombosi, T. I., Sokolov, I. V., et al. 2003, ApJL, 595, L57
Shen, F., Yang, Z., Zhang, J., Wei, W., & Feng, X. 2018, ApJ, 866, 18
Skilling, J. 1971, ApJ, 170, 265
```

```
Sokolov, I. V., van der Holst, B., Oran, R., et al. 2013, ApJ, 764, 23
Sokolov, I. V., van der Holst, B., Manchester, W. B., et al. 2021a, ApJ, 908, 172
```

Sokolov, I. V., Sun, H., Tóth, G., et al. 2021b, JCoPh, submitted Suzuki, T. K., & Inutsuka, S.-I. 2005, ApJL, 632, L49
Tanaka, T. 1994, JCoPh, 111, 381
Tóth, G., Sokolov, I. V., Gombosi, T. I., et al. 2005, JGRA, 110, A12226
Toth, G., van der Holst, B., Sokolov, I. V., et al. 2012, JCoPh, 231, 870
Tu, C.-Y., & Marsch, E. 1997, SoPh, 171, 363

Usmanov, A. V., Goldstein, M. L., Besser, B. P., & Fritzer, J. M. 2000, JGR, 105, 675

Usmanov, A. V., Matthaeus, W. H., Goldstein, M. L., & Chhiber, R. 2018, ApJ, 865, 25

van der Holst, B., Sokolov, I. V., Meng, X., et al. 2014, ApJ, 782, 81

Verdini, A., Velli, M., Matthaeus, W. H., Oughton, S., & Dmitruk, P. 2009, ApJL, 708, L116

Weber, E. J., & Davis, L., Jr. 1967, ApJ, 148, 217

Young, M. A., Schwadron, N. A., Gorby, M., et al. 2021, ApJ, 909, 160